Journal of Solid State Chemistry **166,** 148–157 (2002)
doi:10.1006/jssc.2002.9572, available online at http://www.idealibrary.com on IDEAL®

Layered Intergrowth Phases Bi_4MO_8X (X = Cl, M = Ta, and X = Br, M = Ta or Nb): Structural and Electrophysical Characterization

Ardak M. Kusainova, Wuzong Zhou, John T. S. Irvine, and Philip Lightfoot[1]

School of Chemistry, University of St. Andrews, St. Andrews, Purdie Building, Fife, Scotland KY16 9ST, United Kingdom

Received November 2, 2001; in revised form February 15, 2002; accepted March 1, 2002

The high-temperature structural behavior of the layered intergrowth phase Bi_4TaO_8Cl, belonging to the Sillén-Aurivillius family, has been studied by powder neutron diffraction. This material is ferroelectric, space group $P2_1cn$, at $T_C < 640$ K. An order– disorder transition to centrosymmetric space group *Pmcn* is found around 640 K, which involves disordering of TaO_6 octahedral tilts. A second phase transition, of a first-order nature, to space group *P4/mmm* occurs at a temperature of ~ 1038 K. The crystal structures of the bromide analogs Bi_4MO_8Br (M = Nb, Ta) have also been determined at room temperature; both are isomorphous with Bi_4TaO_8Cl and exhibit maxima in dielectric constant at temperatures of approximately 588 and 450 K, respectively. © 2002 Elsevier Science (USA)

INTRODUCTION

The Aurivillius family of layered bismuth oxides encompasses some of the most widely studied ferroelectrics and oxide-ion conductors of recent years, for example $SrBi_2Ta_2O_9$ (1) and phases based on $Bi_4V_2O_{11}$ (the so-called BIMEVOX family) (2), respectively. The general formula of the Aurivillius phases (3, 4) may be written as $[Bi_2O_2][A_{n-1}B_nO_{3n+1}]$, representing a regular layered intergrowth of fluorite-like $[Bi_2O_2]$ and perovskite-like $[A_{n-1}B_nO_{3n+1}]$ units ($A = Ca^{2+}$, Sr^{2+}, Pb^{2+}, Ln^{3+}, Bi^{3+}; $B = Nb^{5+}$, Ti^{4+}, etc.; n representing the number of "octahedral" perovskite layers). A related series of layered intergrowth phases is the Sillén family, $[M_2O_2][X_m]$ (5, 6), consisting of analogous fluorite-like layers intergrown with halide layers $[X_m]$. Due to the structural similarities of these two families, perhaps it comes as no surprise that a third series of intergrowth phases, combining structural elements of both families, can be prepared (7, 8). These Sillén–Aurivillius intergrowths, in the ideal form, consist of a regular layer sequence $-[Bi_2O_2][A_{n-1}B_nO_{3n+1}][Bi_2O_2][X_m]-$ and may be designated as "$AnXm$" to express the number of perovskite (An) and halide (Xm) layers. This series is represented by its simplest members Bi_4TaO_8Cl ($A1X1$, i.e., $n = 1$, $m = 1$), $Bi_3Pb_2Nb_2O_{11}Cl$ ($A2X1$) (9) and $Bi_5PbTi_3O_{14}Cl$ ($A3X1$) (7). We have recently shown that all of the above phases display ferroelectric properties, and have studied their properties and detailed crystallographic behavior of the ferroelectric phases by powder neutron diffraction (PND) (9, 10).

In the present paper, we extend our studies of the $A1X1$ phases to include a variable temperature PND study of Bi_4TaO_8Cl itself, and also to the crystallographic and preliminary electrical characterization of the bromide analogs Bi_4MO_8Br (M = Nb, Ta). Both the latter compounds are also shown to be ferroelectric-like dielectric maxima, while Bi_4TaO_8Cl is shown to undergo two high-temperature phase transitions, which may be correlated with its ferroelectric behavior, and contrasted with that of the Aurivillius phases.

EXPERIMENTAL

Pure polycrystalline samples of greenish-yellow powders with composition Bi_4MO_8Br, where M = Nb, Ta and yellow powder Bi_4TaO_8Cl were prepared by classical solid state reaction of stoichiometric quantities of BiOCl (Aldrich), BiOBr, Bi_2O_3(Aldrich) and Nb_2O_5 (Aldrich) in evacuated silica tubes at 1180 K for 20 h. BiOBr was prepared by dissolving Bi_2O_3 powder in concentrated 48% HBr acid until saturation and further hydrolysis by adding an excess of boiling water, 1–2 h boiling and stirring, followed by filtering and drying above 393 K. Phase purity was monitored on a Stoe STADI/P powder diffractometer operating in transmission mode and utilizing monochromated $CuK\alpha_1$ radiation.

Powder Neutron Diffraction

Powder neutron diffraction data were collected on the high-resolution powder diffractometer HRPD and the high-intensity powder diffractometer Polaris at the ISIS

[1] To whom the correspondence should be addressed. Fax: 44-1334-463808. E-mail: pl@st-and.ac.uk.

0022-4596/02 $35.00

facility, Chilton, UK. Approximately 10 g samples were packed in cylindrical vanadium cans and data were collected for approximately 2 h each (HRPD) or 1 h each (Polaris). The following data were collected: HRPD—Bi_4TaO_8Cl at temperatures 323, 373, 403, 443, 473, 523, 623 and 773 K; Polaris—Bi_4TaO_8Cl at temperatures 298, 773, 823, 873, 923, 973 and 1023 K, Bi_4NbO_8Br and Bi_4TaO_8Br at 298 K. The ISIS source operates in energy-dispersive (time-of-flight) mode, with scattered neutrons being detected at fixed detector banks centered at $2\theta = 90$ and 168° (for HRPD) or $2\theta = 90$ and 145° (for Polaris). In the case of HRPD, only the data from the 168° (high-resolution) banks were used for Rietveld refinement; for Polaris, both detector banks were used. The Rietveld refinement was carried out using the GSAS package (11).

Dielectric Measurements

Impedance measurements were performed using a Solartron 1260 frequency response analyzer, using Z plot and Z view impedance software (Scribner). Pellets in the form of disks with $d = 8$ mm and of 2–3 mm thickness were obtained by pressing (3 t) powders of Bi_4NbO_8Br and Bi_4TaO_8Br with a little addition of polyvinylalcohol, 3% solution. Pellets suitable for electrophysical measurements were sintered at 850 K for 5 h in air. Maximum sample densities achievable were approximately 60% of theoretical value. After heating all pellets were checked by X-ray powder diffraction, which showed that both materials are chemically stable in this range of temperatures. Electrodes with electrical resistance 2–5 Ω were put on both sides of the pellets by Au-paste (Engelhard) painting and annealing at 900 K. Dielectric constant and electrical conductivity were measured between 408 and 770 K with a PC-controlled Solartron 1260 impedance analyzer in the frequency range 10^{-1}–10^{7} Hz.

Electron Microscopy

High-resolution transmission electron microscope (HRTEM) images and selected area electron diffraction (SAED) patterns were obtained on a Jeol JEM-2010 electron microscope operating at 200 kV. Specimens were prepared by gently grinding the powder sample in acetone and spreading it on a holey carbon film supported on a Cu grid. The HRTEM images were recorded at a magnification of 800,000 ×.

Thermal Analysis

Differential Thermal Analysis (DTA) measurements were performed using TA instruments 2960. The samples were packed in alumina crucibles, and treated in a flow of N_2 gas (flow rate 72 mL/min) in the temperature range 20–1000°C (heating rate 10°C/min).

RESULTS AND DISCUSSION

Variable Temperature Structural Study of Bi_4TaO_8Cl

Our previous analysis of the crystal structure of Bi_4TaO_8Cl and Bi_4NbO_8Cl (10) confirmed that the model originally proposed by Ackerman (8) for Bi_4NbO_8Cl, from single-crystal X-ray diffraction data, was correct, with a complex lowering of symmetry from the ideal "parent" structure (tetragonal, $P4/mmm$, $a \sim 3.9$ Å, $c \sim 14.4$ Å) to a polar orthorhombic phase ($P2_1cn$, $a \sim 5.45$ Å, $b \sim 5.49$ Å, $c \sim 28.8$ Å; i.e., $a\ \sqrt{2}a \times \sqrt{2}a \times 2c$ superstructure). This lowering of symmetry arises from a considerable degree of distortion and tilting of the TaO_6 octahedra within the perovskite block, together with a large displacement of several atoms along the polar a-axis (Fig. 1). In commencing this study, we therefore proceeded to use this model in all refinements below the previously determined T_C of 640 K. The model consisted of isotropic thermal parameters for all atoms, lattice parameters, and parameters to model the pseudo-Voigt peak shape and background function. Good-quality fits were obtained for this model for both the HRPD and Polaris refinements. It was anticipated that at T_C the structure might undergo a continuous phase transition towards the tetragonal "parent" phase. However, this was soon found to be not the case. Analysis of the Polaris data for the 773–973 K runs clearly showed that a considerable orthorhombic distortion was still present. Indeed, the degree of orthorhombic distortion, defined as $2(b - a)/(b + a)$, was found to change little over this temperature range, displaying only a slight maximum around T_C (Fig. 2). Moreover, key weak reflections demonstrating the doubling of the c-axis were also still present. In stark contrast, refinement

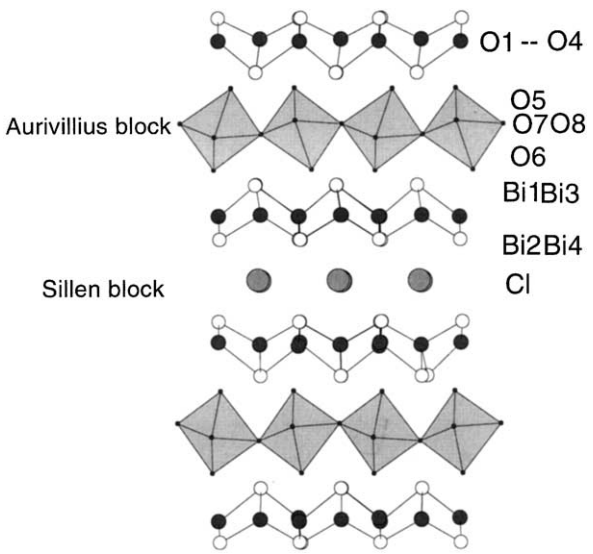

FIG. 1. Crystal structure of the paraelectric phase of Bi_4MO_8X, space group $P2_1cn$, showing the regular intergrowth of Aurivillius and Sillén blocks.

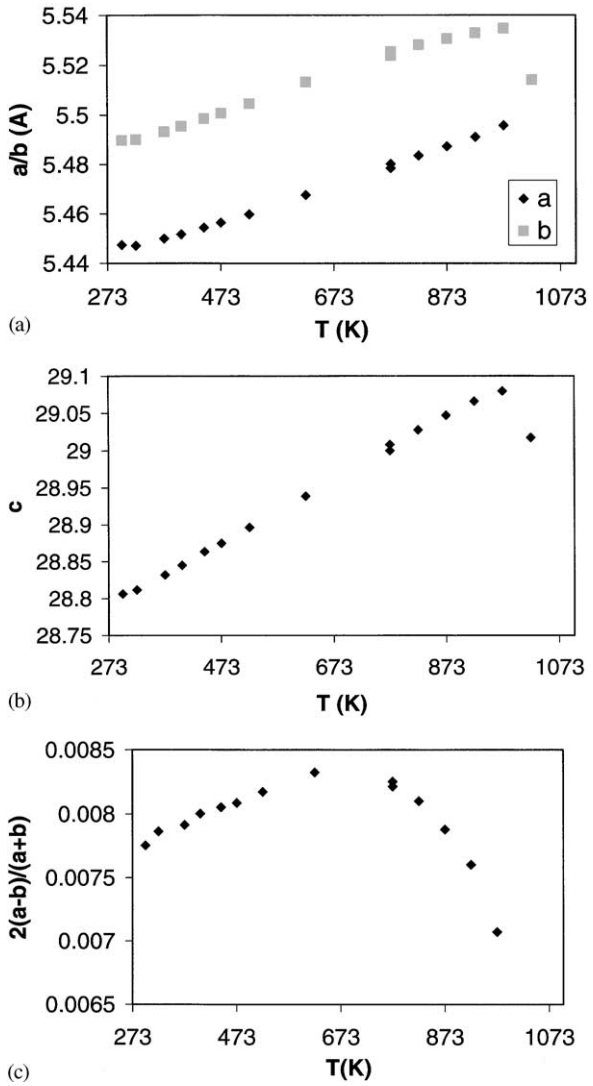

FIG. 2. Thermal evolution of unit cell parameters for Bi_4TaO_8Cl (a) a/b parameters (b) c-parameter, and (c) orthorhombicity.

of the data at 1023 K did show a dramatic reduction in orthorhombicity—in fact, although very weak reflections violating the parent tetragonal symmetry were still observable in this dataset, the orthorhombic refinements were unstable, and led to poorer agreement factors than a refinement in the parent $P4/mmm$ model. The crystallographic data presented here, together with the previous knowledge of the centrosymmetric nature of the structure above 640 K, from SHG and dielectric data (10), prompt us to conclude the following sequence of phases for Bi_4TaO_8Cl:

$$\begin{array}{ccccc} & \sim 640\ \text{K} & & \sim 1038\ \text{K} & \\ P2_1cn & \longrightarrow & Pmcn & \longrightarrow & P4/mmm \\ \sqrt{2}a \times \sqrt{2}a \times 2c & & \sqrt{2}a \times \sqrt{2}a \times 2c & & a \times a \times c \end{array}$$

The variation of the lattice parameters with temperature, in particular, the dramatic coalescence of a/b at 1023 K and

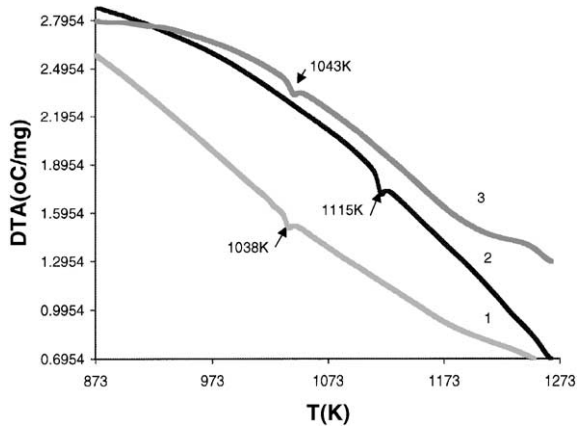

FIG. 3. DTA traces for (1) Bi_4TaO_8Cl, (2) Bi_4NbO_8Br and (3) Bi_4TaO_8Br.

the discontinuous decrease in c at the same temperature signifies a first-order orthorhombic–tetragonal phase transition. This conclusion is supported by the observation of a sharp endotherm in the DTA trace at that temperature (Fig. 3). We also note that no DTA peak is observed corresponding to T_C, compatible with a second-order transition at that point.

Refinement of the Polaris datasets at 773, 823, 873, 923 and 973 K was, therefore, carried out in the centrosymmetric space group $Pmcn$, whilst that at 1023 K was carried out in the parent tetragonal model, $P4/mmm$. Final refined atomic parameters for models selected within each of the three regimes are given in Tables 1–3, and selected bond distances and angles in Table 4.

For the $Pmcn$ refinements, it soon became apparent that there was considerable disorder at several of the atomic sites, in particular, the apical sites of the TaO_6 octahedra,

TABLE 1
Refined Structural Parameters for Bi_4TaO_8Cl at 623 K, Space Group $P2_1cn$, $a = 5.4676(1)$ Å, $b = 5.5133(1)$ Å, $c = 28.9382(6)$ Å

Atom	x	y	z	U_{iso} ($\times 100$)
Ta(1)	0.023(4)	0.238(2)	0.2528(5)	1.4(2)
Bi(1)	0.0	0.812(2)	0.1580(5)	3.8(4)
Bi(2)	0.016(3)	0.253(2)	0.4316(3)	2.7(2)
Bi(3)	0.031(3)	0.772(2)	0.3421(3)	3.9(2)
Bi(4)	0.031(3)	0.259(2)	0.0684(3)	1.2(2)
Cl(1)	0.509(5)	0.242(2)	0.0001(5)	4.2(1)
O(1)	0.767(5)	0.480(3)	0.3960(5)	2.5(5)
O(2)	0.255(5)	0.513(3)	0.3956(4)	1.1(4)
O(3)	0.750(5)	0.017(3)	0.3900(4)	0.9(3)
O(4)	0.259(5)	− 0.016(3)	0.3963(4)	3.5(4)
O(5)	0.425(4)	0.687(2)	0.3179(5)	1.7(3)
O(6)	0.585(6)	0.737(5)	0.1842(9)	8.8(7)
O(7)	0.245(5)	− 0.031(3)	0.2365(6)	4.3(5)
O(8)	− 0.265(6)	0.016(4)	0.2603(8)	7.0(8)

$\chi^2 = 2.6$, $R_{wp} = 0.056$, for 65 variables, d-spacing range $0.66 < 2.48$ Å.

TABLE 2

Refined Structural Parameters for Bi_4TaO_8Cl at 973 K, Space Group *Pmcn*, $a = 5.4952(2)$ Å, $b = 5.5344(2)$ Å, $c = 29.0786(8)$ Å

Atom	x	y	z	U_{iso} ($\times 100$)
Ta(1)	0.25	0.2417(9)	0.2544(2)	0.73(8)
Bi(1)	0.25	0.798(2)	0.1560(2)	2.9(2)
Bi(2)	0.25	0.258(2)	0.4319(2)	1.9(1)
Bi(3)	0.25	0.779(2)	0.3375(2)	4.2(2)
Bi(4)	0.25	0.254(1)	0.0700(2)	1.3(1)
Cl(1)	0.75	0.247(3)	0.0041(3)	4.2[a]
O(1)	0.008(1)	0.494(1)	0.3935(3)	2.8[a]
O(2)	0.007(1)	0.004(2)	0.3934(3)	2.0[a]
O(3)[b]	0.862(1)	0.679(1)	0.3129(3)	1.1(2)
O(4)[b]	0.793(2)	0.728(2)	0.1817(3)	3.5(3)
O(5)	0.494(2)	− 0.031(2)	0.2438(6)	10.2[a]

Atom	U_{11}($\times 100$)	U_{22}	U_{33}	U_{12}	U_{13}	U_{23}
Cl(1)	5.5(3)	4.8(2)	2.4(3)	0	0	1.0(4)
O(1)	3.2(4)	0.7(3)	4.3(5)	− 0.6(2)	0.1(4)	− 1.0(3)
O(2)	0.8(3)	2.9(4)	2.2(4)	− 1.5(2)	1.0(3)	0.4(3)
O(5)	5.9(4)	4.5(4)	20(1)	5.1(3)	6.1(8)	− 2.6(8)

Note. $\chi^2 = 3.0$, $R_{wp} = 0.022$, for 78 variables, d-spacing range $0.48 < 4.2$ Å.

[a] Refined anisotropically.

[b] Atoms disordered about $x = 0.75$: occupancy = 0.5.

O(3) and O(4). Anisotropic refinement of these two atoms resulted in unreasonably elongated U_{11} parameters, indicative of severe local disorder at these sites, i.e., an order–disorder transition occurs on passing from the polar phase to the centrosymmetric orthorhombic phase, with cooperative tilts and displacements still occurring around the octahedral layers, but no long-range polar order is now present. The best refinements of this phase were obtained by allowing 50:50 disorder of O(3) and O(4) around the mirror plane at $x = 0.75$, together with anisotropic refinement of the remaining oxygen and chlorine sites. Interestingly, these refinements do give slightly poorer agreement factors than those in the polar space group $P2_1cn$ (e.g., $\chi^2 = 2.6$ for *Pmcn*

TABLE 3

Refined Structural Parameters for Bi_4TaO_8Cl at 1023 K, Space Group *P2/mmm*, $a = 3.8991(1)$ Å, $c = 14.5104(4)$ Å

Atom	x	y	z	U_{11} ($\times 100$)	U_{22} ($\times 100$)	U_{33} ($\times 100$)
Ta(1)	0	0	0	0.85(8)	0.85(8)	2.1(2)
Bi(1)	0	0	0.3614(1)	1.76(5)	1.76(5)	2.3(1)
Bi(2)	0.5	0.5	0.1820(2)	7.0(1)	7.0(1)	3.6(1)
Cl(1)	0.5	0.5	0.5	4.8(1)	4.8(1)	4.6(2)
O(1)	0	0.5	0.2859(1)	2.6(1)	1.6(1)	3.1(1)
O(2)	0	0	0.1341(3)	18.4(3)	18.4(3)	2.1(2)
O(3)	0	0.5	0	9.6(4)	0.0(1)	21.4(5)

$\chi^2 = 2.8$, $R_{wp} = 0.022$, for 40 variables, d-spacing range $0.48 < 4.2$ Å.

TABLE 4

Selected Bond Distances and Angles for Bi_4TaO_8Cl (I), Bi_4NbO_8Br (II), and Bi_4TaO_8Br (III) in the Ferroelectric Phase ($P2_1cn$)

	I—298 K	I—623 K	II—298 K	III—298 K
M(1)–O(5)	2.04(1)	2.13(2)	2.01(1)	2.08(1)
M(1)–O(6)	1.95(2)	1.85(3)	2.03(1)	1.95(1)
M(1)–O(7)	2.03(1)	1.97(3)	1.92(1)	1.91(1)
	1.95(1)	2.01(3)	2.08(1)	2.05(1)
M(1)–O(8)	2.08(1)	2.01(3)	2.18(1)	2.15(1)
	1.89(1)	1.96(3)	1.89(1)	1.83(1)
Bi(1)–O(1)	2.30(1)	2.33(2)	2.24(1)	2.31(1)
Bi(1)–O(2)	2.23(1)	2.33(2)	2.23(1)	2.20(1)
Bi(1)–O(3)	2.73(1)	2.54(2)	2.76(1)	2.64(1)
Bi(1)–O(4)	2.65(1)	2.73(2)	2.61(1)	2.70(1)
Bi(1)–O(5)	2.19(1)	2.22(1)	2.13(1)	2.08(1)
Bi(1)–O(6)	2.38(1)	2.43(3)	2.46(1)	2.42(1)
Bi(1)–O(7)	2.99(1)	2.78(3)	3.04(1)	3.10(1)
Bi(1)–O(8)	3.24(1)	3.15(3)	3.32(1)	3.30(1)
Bi(2)–Cl/Br(1)	3.26(1)	3.41(2)	3.45(1)	3.46(1)
	3.36(1)	3.35(2)	3.56(1)	3.51(1)
	3.40(1)	3.45(2)	3.46(1)	3.39(1)
	3.38(1)	3.34(2)	3.45(1)	3.47(1)
Bi(2)–O(1)	2.24(1)	2.12(2)	2.21(1)	2.28(1)
Bi(2)–O(2)	2.17(1)	2.20(2)	2.14(1)	2.17(1)
Bi(2)–O(3)	2.19(1)	2.30(2)	2.10(1)	2.24(1)
Bi(2)–O(4)	2.29(1)	2.24(2)	2.41(1)	2.27(1)
Bi(3)–O(1)	2.57(1)	2.67(3)	2.46(1)	2.64(1)
Bi(3)–O(2)	2.51(1)	2.44(2)	2.34(1)	2.54(1)
Bi(3)–O(3)	2.44(1)	2.47(2)	2.63(1)	2.49(1)
Bi(3)–O(4)	2.23(1)	2.32(2)	2.40(1)	2.19(1)
Bi(3)–O(5)	2.29(1)	2.31(2)	2.28(1)	2.33(1)
Bi(3)–O(6)	2.50(1)	2.69(3)	2.73(1)	2.51(1)
Bi(3)–O(7)	2.98(1)	3.23(2)	3.14(1)	2.93(1)
Bi(3)–O(8)	2.84(1)	3.17(3)	2.87(1)	2.78(1)
Bi(4)–Cl/Br(1)	3.41(1)	3.47(2)	3.30(1)	3.34(1)
	3.37(1)	3.28(2)	3.44(1)	3.46(1)
	3.38(1)	3.40(2)	3.46(1)	3.57(1)
	3.31(1)	3.40(2)	3.46(1)	3.42(1)
Bi(4)–O(1)	2.17(1)	2.26(2)	2.25(1)	2.22(1)
Bi(4)–O(2)	2.27(1)	2.28(2)	2.32(1)	2.30(1)
Bi(4)–O(3)	2.19(1)	2.22(2)	2.29(1)	2.18(1)
Bi(4)–O(4)	2.24(1)	2.20(2)	2.18(1)	2.17(1)
O(5)–*M*(1)–O(6)	166.9(4)	171(2)	157.5(4)	163.7(4)
O(5)–*M*(1)–O(7)	82.9(4)	80(1)	101.2(4)	103.8(4)
	98.4(5)	92(1)	83.2(4)	79.5(4)
O(5)–*M*(1)–O(8)	81.9(4)	80(1)	82.4(4)	81.1(4)
	96.0(4)	94(1)	94.9(4)	97.8(4)
O(6)–*M*(1)–O(7)	89.8(5)	97(1)	61.1(4)	66.3(4)
	91.1(5)	89(1)	117.2(4)	112.1(1)
O(6)–*M*(1)–O(8)	87.1(6)	92(1)	81.5(4)	84.9(4)
	92.0(6)	95(1)	92.9(4)	93.2(4)
O(7)–*M*(1)–O(7)	167.3(6)	168(1)	166.7(7)	172.2(5)
O(7)–*M*(1)–O(8)	88.0(4)	93(1)	83.0(6)	84.5(4)
	71.9(4)	100(1)	73.0(3)	80.1(3)
	104.7(4)	77(1)	110.0(4)	103.1(3)
	95.5(5)	89(1)	94.3(6)	92.5(5)
O(8)–*M*(1)–O(8)	159.9(6)	164(1)	154.9(6)	163.9(5)
M(1)–O(7)–*M*(1)	153(2)	155(5)	154.7(5)	157.3(3)
M(1)–O(8)–M(1)	154(2)	157(2)	146.5(5)	154.3(4)

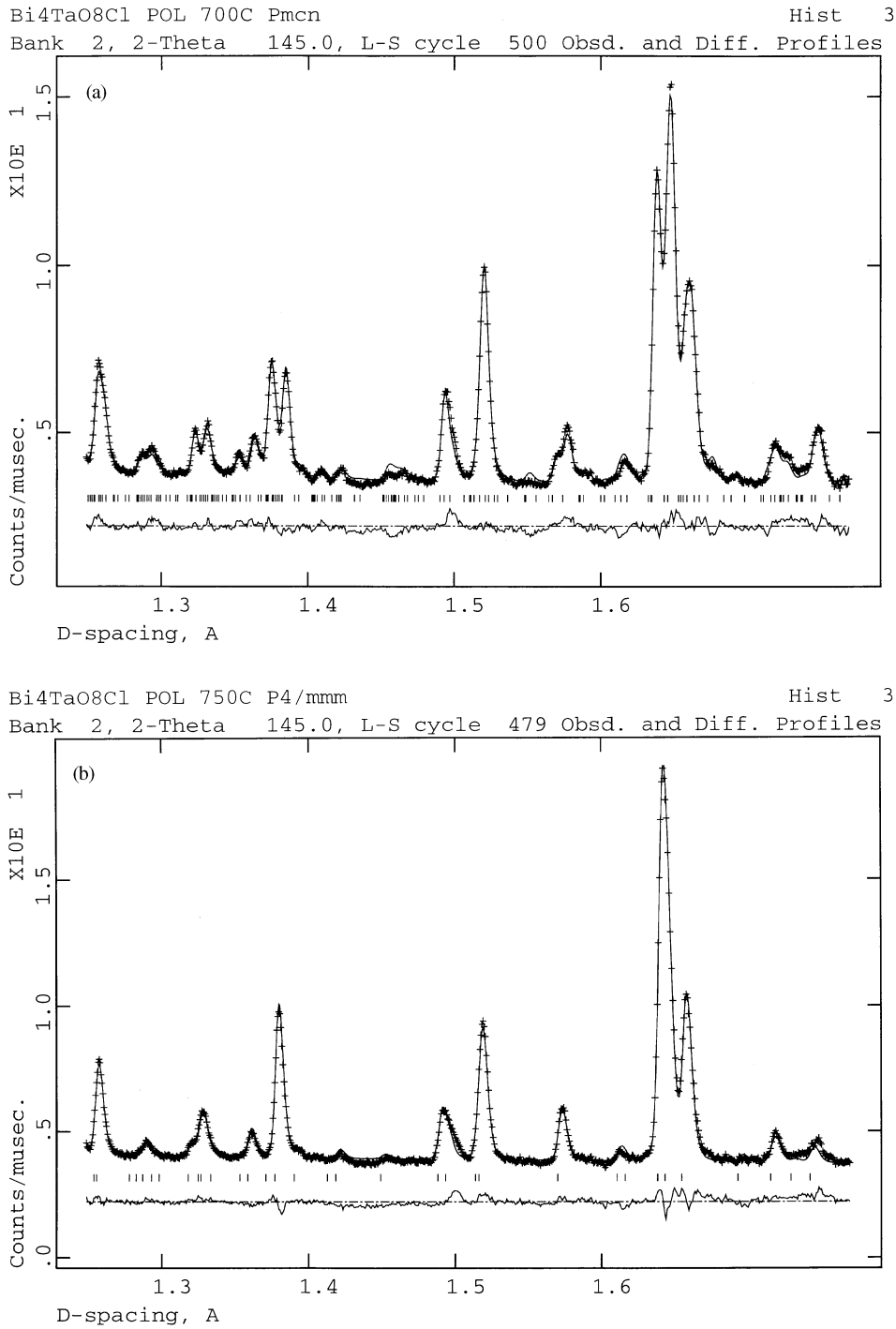

FIG. 4. Portion of the final Rietveld fits for Bi_4TaO_8Cl at (a) 973 K (*Pmcn* model) and (b) 1023 K (*P*4/*mmm* model).

vs 2.9 for $P2_1cn$ at 823 K), but these differences must be regarded as insignificant bearing in mind the SHG and dielectric measurements, and the difficulties in obtaining a fully anisotropic structural model from powder diffraction data.

The refinement of the 1023 K dataset proceeded straightforwardly in the tetragonal model, allowing anisotropic thermal parameters for all atoms. It can also be noted from this that a considerable degree of local displacement around the TaO_6 octahedra still exists (e.g. U_{11} and U_{33} parameters for O(2) and O(3), respectively). The clear differences in symmetry between 973 and 1023 K, as modelled by the *Pmcn* and *P*4/*mmm* phases, are best seen in the highlighted regions of the Rietveld plots in Fig. 4.

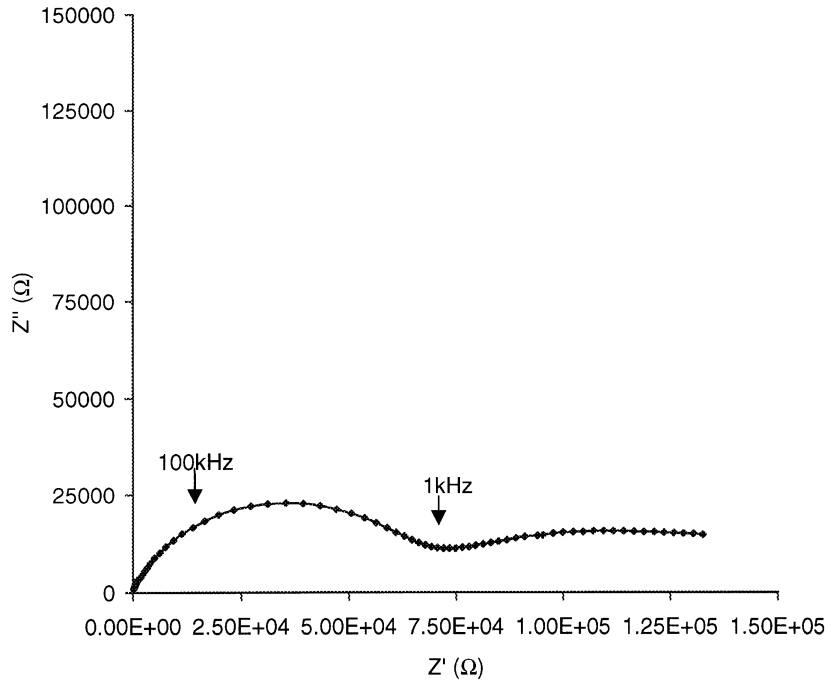

FIG. 5. Impedance plot for Bi_4NbO_8Br at 633 K.

Although the observation of an intermediate paraelectric orthorhombic (*Pmcn*) phase in Bi_4TaO_8Cl was unexpected, it is perhaps not entirely surprising. Our recent variable temperature PND study of the $n = 2$ Aurivillius phase $Sr_{0.85}Bi_{2.1}Ta_2O_9$ (12) also revealed an intermediate orthorhombic paraelectric phase, although in that case it was ascribed to the "freezing-out" of a particular octahedral tilt mode rather than to an order–disorder transition. Interest-

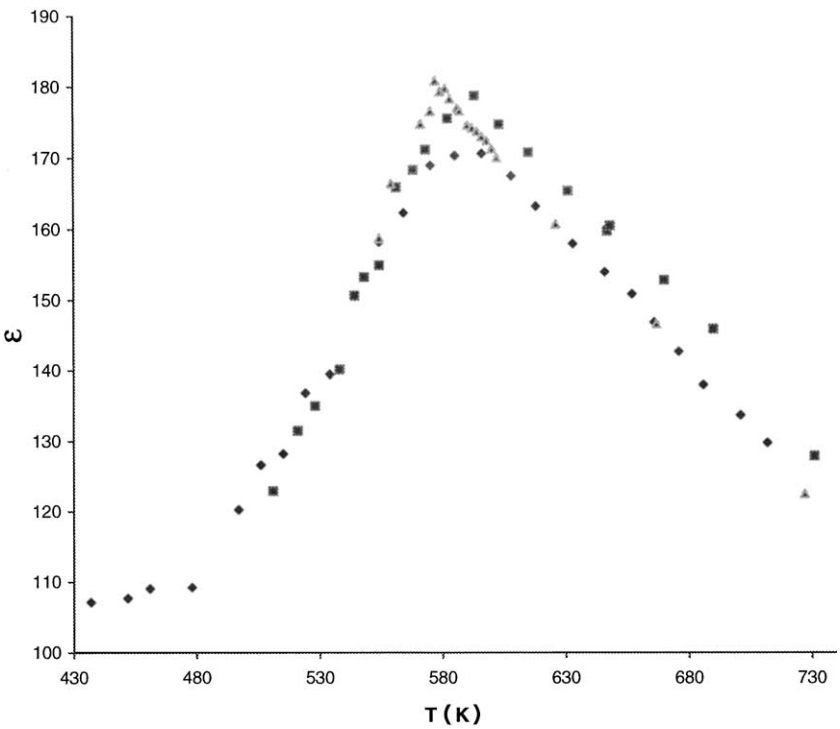

FIG. 6. Temperature dependence of dielectric constant for Bi_4NbO_8Br: square—heating, triangle—cooling, diamond—reheating.

ingly, we have also evidenced a third type of phase-transition behavior in the $n = 3$ Aurivillius phase $Bi_4Ti_3O_{12}$ (13, 14), which shows a single phase transition at T_C directly from a polar orthorhombic to a paraelectric tetragonal phase. This rich structural phase-transition behavior in these layered intergrowth families is clearly worthy of further investigation.

Electrical Characterization of Bi_4NbO_8Br and Bi_4TaO_8Br

Previous studies (10) have shown that Bi_4NbO_8Cl and Bi_4TaO_8Cl are ferroelectrics, with Curie transitions at 765 and 640 K, respectively. When measured at a frequency of 1 MHz, the permittivities at the transition temperature are 150 and 110 for Bi_4NbO_8Cl and Bi_4TaO_8Cl, respectively.

In this study we have investigated the analogous Br compounds using ac impedance spectroscopy to give a less frequency-dependent set of data. A typical impedance response for Bi_4NbO_8Br is shown in Fig. 5. By fitting the dielectric relaxation on the left-hand side of the Figure, i.e., high frequency, we are able to obtain a good estimate of the permitivity of the material. The permittivity of Bi_4NbO_8Br shows a pronounced ferroelectric-like behavior, Fig. 6. The maximum in permittivity occurs at 588 K, with a value of 180. This is reversible upon heating and cooling cycles.

The behavior of Bi_4TaO_8Br is somewhat more difficult to study as its dielectric anomaly is at lower temperatures and the resistivity is significantly higher. Therefore, the variation in permittivity with frequency was examined. Representative data corresponding to around 1 MHz are presented in Fig. 7. Here the maximum in permittivity is around 195 at a temperature of about 450 K.

Room-Temperature Crystal Structure of Bi_4NbO_8Br and Bi_4TaO_8Br

Preliminary examination of the powder X-ray diffraction data suggested that the oxybromides were essentially isomorphous with the corresponding chlorides. These structures can be described, as discussed previously, as regular intergrowths of alternating fluorite-like, halide and perovskite-like blocks (Fig. 1). The fluorite-like block consists of fairly regular edge-sharing OBi_4 tetrahedra, which are common to both Sillén and Aurivillius phases, and also occur, for example, in the $MOCuX$ family of complex oxides, oxyhalides and oxychalcogenides (15). The perovskite-like blocks in the present phases consist of a single octahedral MO_6 layer which is markedly distorted, in contrast to that observed in the $n = 2$ analog, $Bi_3Pb_2Nb_2O_{11}Cl$ (9). These distortions are further discussed below.

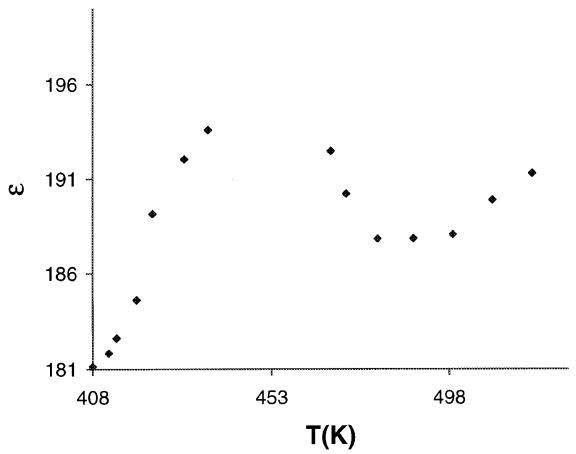

FIG. 7. Temperature dependence of dielectric constant for Bi_4TaO_8Br.

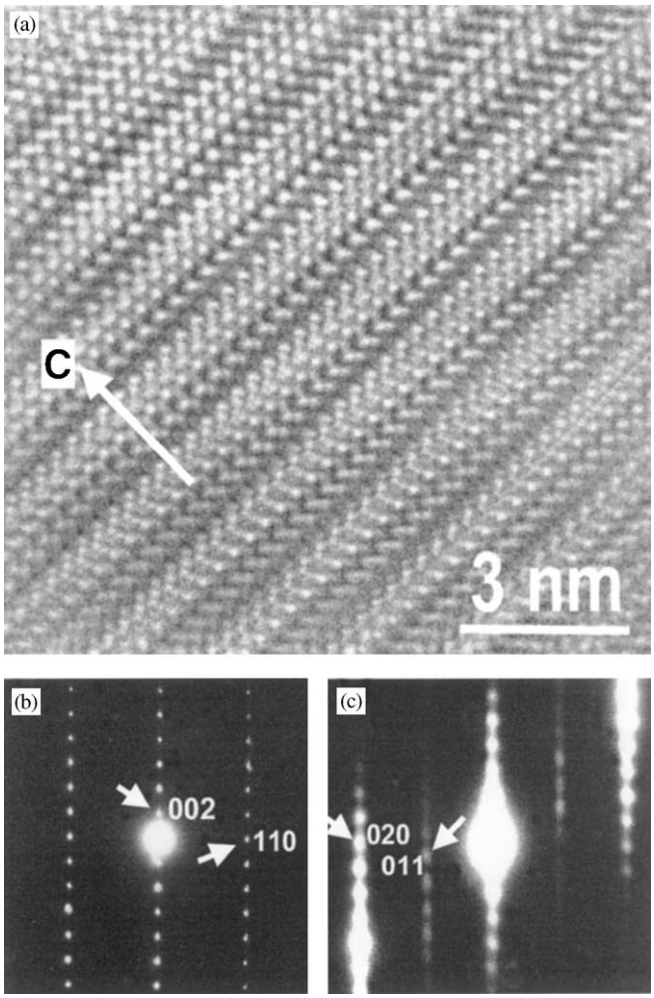

FIG. 8. HRTEM image (a) and the corresponding SAED pattern (b) of Bi_4NbO_8Br viewed down the $[1\bar{1}0]$ direction; c-axis is indicated. (c) SAED pattern along the [100] zone axis. Both SAED patterns are indexed on the $\sqrt{2}a \times \sqrt{2}b \times 2c$ unit cell.

The unit cell of Bi_4NbO_8Br was confirmed by HRTEM. Figures 8a and 8b show an HRTEM image and the corresponding SAED pattern viewed down the $[1\bar{1}0]$ zone axis of the $\sqrt{2}a \times \sqrt{2}b \times 2c$ unit cell. Neither defects nor further superlattice was observed. Figure 8c is an SAED pattern

TABLE 5

Refined Structural Parameters for Bi_4MO_8Br at 298 K, Space Group $P2_1cn$ (M = Nb, First Line; M = Ta, second line): II. Bi_4NbO_8Br: a = 5.4846(2) Å, b = 5.5334(1) Å, c = 29.0951(9) Å and III. Bi_4TaO_8Br: a = 5.4710(1) Å, b = 5.5172(1) Å, c = 29.2241(8) Å

Atom	x	y	z	U_{iso} ($\times 100$)
M(1)	− 0.011(2)	0.249(1)	0.2502(2)	0.15(3)
	0.018(2)	0.2398(7)	0.2500(3)	0.18(4)
Bi(1)	0.0	0.8150(9)	0.1591(2)	1.28(5)
	0.0	0.8189(7)	0.1587(2)	1.18(4)
Bi(2)	− 0.010(2)	0.2515(8)	0.4269(1)	0.23(3)
	0.019(2)	0.2440(7)	0.4283(2)	0.34(2)
Bi(3)	0.026(2)	0.7201(9)	0.3405(2)	1.28(5)
	0.030(1)	0.7803(7)	0.3398(2)	1.18(4)
Bi(4)	− 0.012(1)	0.2513(8)	0.0692(1)	0.23(3)
	0.010(2)	0.2631(8)	0.0711(2)	0.34(2)
Br(1)	0.503(2)	0.2494(9)	0.0020(5)	1.02(6)
	0.524(2)	0.254(1)	0.0021(2)	0.79(6)
O(1)	0.740(2)	0.506(1)	0.3916(2)	0.15(3)
	0.756(2)	0.505(1)	0.3933(3)	0.23(2)
O(2)	0.244(2)	0.478(1)	0.3918(2)	0.15(3)
	0.260(2)	0.492(1)	0.3921(3)	0.23(2)
O(3)	0.763(2)	− 0.003(1)	0.3947(2)	0.15(3)
	0.750(2)	0.009(1)	0.3915(2)	0.23(2)
O(4)	0.266(2)	− 0.015(1)	0.3873(2)	0.15(3)
	0.255(2)	− 0.022(1)	0.3890(2)	0.23(2)
O(5)	0.416(2)	0.666(1)	0.3155(3)	1.53(8)
	0.423(2)	0.665(1)	0.3174(3)	1.22(7)
O(6)	0.589(2)	0.692(2)	0.1835(3)	1.53(8)
	0.596(2)	0.710(1)	0.1850(3)	1.22(7)
O(7)	0.259(3)	0.038(2)	0.2628(3)	1.9(1)
	0.276(2)	0.016(1)	0.2625(2)	1.15(7)
O(8)	− 0.224(2)	− 0.076(2)	0.2632(3)	1.9(1)
	− 0.217(2)	− 0.066(1)	0.2617(2)	1.15(7)

Note. U_{iso} for Bi(1)/Bi(3), Bi(2)/Bi(4), O(1)–O(4), O(5)/O(6) and O(7)/O(8) were constrained equal. II. $\chi^2 = 3.8$, $R_{wp} = 0.040$, for 69 variables, d-spacing range 0.40 < 4.2 Å. III. $\chi^2 = 5.2$, $R_{wp} = 0.036$, for 69 variables, d-spacing range 0.40 < 4.2 Å.

along the [100] direction. Indexing is given based on the $\sqrt{2}a \times \sqrt{2}b \times 2c$ unit cell; the presence of the 01l reflections (l odd) clearly confirming the doubled c-axis.

For refinement of the PND data, the same starting model, in space group $P2_1cn$, was used for both bromides. In addition to the weak superlattice peaks observed in the electron diffraction data, direct support for this model was also obtained from the quality of the fits for this model. Due to the markedly lower resolution of Polaris vs HRPD and the high degree of pseudosymmetry, it was not possible to refine individual isotropic thermal parameters for all atoms. Hence, thermal parameters of "similar" atoms were constrained to be equal, as presented in Table 5. Good-quality fits for both materials were again obtained. Final bond distances and angles for the two bromides are compared with those of Bi_4TaO_8Cl in Table 4. A final Rietveld fit for Bi_4TaO_8Br is given in Fig. 9.

DTA measurements on the two bromides (Fig. 3) show endothermic events at temperatures much higher than the Curie temperatures revealed by the ac impedance studies. This suggests that these two compounds also undergo two sequential phase transitions of a type similar to those observed for Bi_4TaO_8Cl. Structurally, Bi_4NbO_8Br and Bi_4TaO_8Br display very similar distortions to their chloride analogs. It can be seen, for example, that the nature of the distortion of the MO_6 octahedra is the same in each case —M is displaced off-center towards a *face* of the octahedron rather than towards an apex, as is found in the $A2X1$ phase $Bi_3Pb_2Nb_2O_{11}Cl$ (9). Also, the distortion around the Bi sites within the $[Bi_2O_2]$ layer is similar—the Bi^{3+} lone-pair is stereochemically active in elongating the *extra*-layer Bi–X and Bi–O bonds, while the *intra*-layer Bi–O bonds remain short. We note, as an additional subtlety, that the intra-layer bonds from the Bi(2) and Bi(4) sites, which are additionally bonded to the halide layers are, on average, significantly shorter, and more evenly distributed than the intra-layer bonds from the Bi(1) and Bi(3) sites, which are also bonded to the apical sites of the perovskite blocks. This anisotropy of the bonding around the oxygen site within the $[Bi_2O_2]$ layer is carried through to the high-temperature tetragonal phase—Bi(1)–O(1) = 2.236(1), Bi(2)–O(1) = 2.465(2) Å.

In order to try to pinpoint the essential structural differences in detail between the three phases, we may calculate the degree of distortion of individual polyhedral units, for example, the perovskitic MO_6 octahedra and the fluorite-like OBi_4 tetrahedra. Distortion indices may be defined as

$$\beta_{oct} = \sum |r_i - r_{av}|/6, \qquad \beta_{tet} = \sum |r_i - r_{av}|/4,$$

where r_i is an individual M–O bond length, r_{av} is the mean (6 for oct, 4 for tet).

$$\alpha_{oct} = \sum |\theta_i - 90|/12, \qquad \alpha_{tet} = \sum |\theta_i - 109|/6,$$

where θ_i is an individual O–M–O or Bi–O–Bi bond angle (12 for oct, 6 for tet).

For each of the three phases, these values are presented in Table 6. From these values, it can be suggested that the replacement of Cl^- by Br^- in these structures leads to a slightly larger distortion of the MO_6 octahedra, but an insignificant difference in the distortion of the $[Bi_2O_2]$ layers. This can be understood by comparing the a/b lattice parameters of the corresponding Aurivillius and Sillén phases Bi_2NbO_5F (16), BiOCl (17) and BiOBr (18) which, taken as the "$a\sqrt{2}$" parameters of the tetragonal cell, are 5.42, 5.50 and 5.55 Å, respectively. The current lattice parameters lie closest to those of the latter materials. This implies that the lattice parameters of the $A1X1$ phases studied here are predominantly determined by the requirement to accommodate the Sillén unit, and that the MO_6 octahedral layer is under considerable tensile stress in order

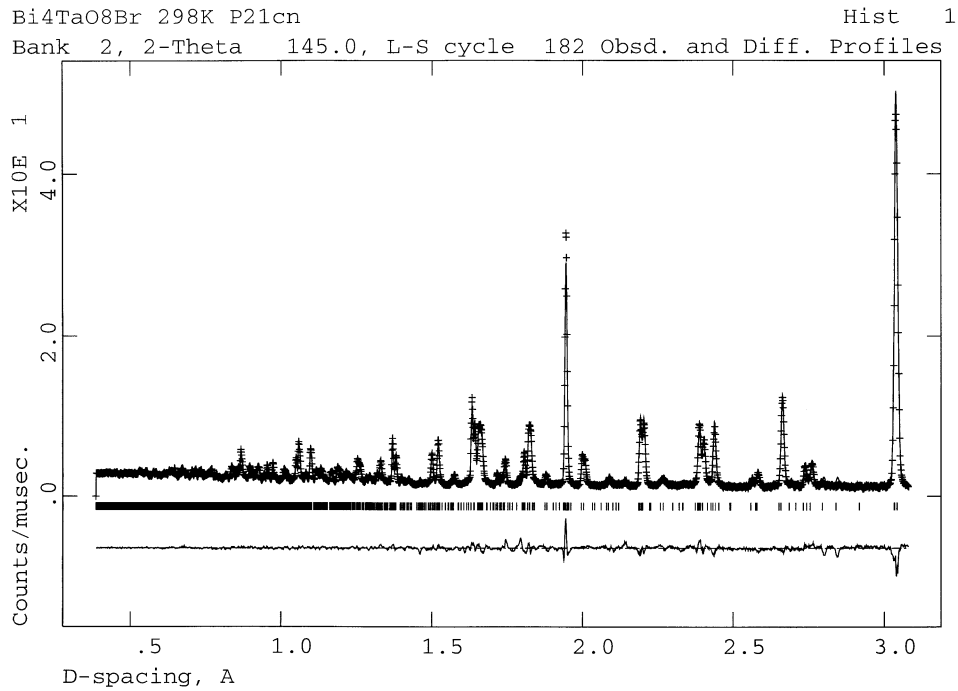

FIG. 9. Final Rietveld fit for Bi_4TaO_8Br at 298 K (space group $P2_1cn$).

to accommodate the intergrowth with the "wider" halide block. The enhanced octahedral distortions observed result from this requirement.

An alternative method of viewing the degree of distortion within the three phases, and its possible influence on dielectric properties, is to calculate the total spontaneous polarization, based on a simple ionic model (19). In the ferroelectric phase, space group $P2_1cn$, a is the polar axis—there is no net polarization along the b- or c-axis, as the presence of the planes of symmetry leads to a cancellation of the individual atomic displacements. In order to calculate the total polarization along a, the contribution of each constituent ion is summed according to

$$P_s = 1/V \sum_i (m_i \Delta x_i q_i e),$$

where P_s is the net spontaneous polarization, V is the unit cell volume, m_i is the site multiplicity, Δx_i is the atomic displacement (Å) along the a-axis relative to the "ideal" tetragonal structure and $q_i e$ is the ionic charge, in Coulombs. Application of this formula to phases I, II and III at 298 K gives P_s values of 2.9, 6.0 and 1.8 $\mu C/cm^2$, respectively. In each case, the biggest individual displacements from ideality occur within the MO_6 octahedron (particularly the O(5) and O(6) apical sites, due to the octahedral tilt mode—however, these partially cancel each other). However, although it is clear that the Nb-containing phase has a significantly larger calculated polarization than the Ta compounds, it is not possible to pinpoint the key parameters responsible for the ferroelectric effect from these data. In particular, there does not seem to be any straightforward correlation of T_C vs octahedral atom displacement or calculated P_s, of the type suggested by earlier work (20, 21).

TABLE 6
Polyhedral Distortion Parameters[a] for Bi_4TaO_8Cl (I), Bi_4NbO_8Br (II), and Bi_4TaO_8Br (III)

Sample	β_{oct} (Å)	β_{tet} (Å)[b]	α_{oct} (deg)	α_{tet} (deg)[b]
I	0.06	0.13, 0.11, 0.20, 0.15	6.3	5.0, 9.0, 4.3, 5.2
II	0.08	0.09, 0.07, 0.25, 0.11	12.2	6.7, 7.7, 5.3, 5.8
III	0.10	0.14, 0.12, 0.18, 0.18	10.5	6.7, 8.3, 5.5, 5.3

[a] See text for definitions.
[b] For O(1), O(2), O(3) and O(4), respectively.

CONCLUSIONS

We have shown that, in addition to our earlier work on the $A1X1$ and $A2X1$ chlorides, that the $A1X1$ bromides, Bi_4NbO_8Br and Bi_4TaO_8Br, also appear to possess ferroelectric properties. This suggests that ferroelectricity should be as widespread in this family of intergrowth compounds as it is in the Aurivillius phases themselves and, moreover, the additional chemical and structural degrees of freedom may offer additional flexibility and control of the particular ferroelectric properties obtainable within the general field of layered perovskites. We have also shown that the ferroelectric–paraelectric phase transition in the $A1X1$

phase Bi_4TaO_8Cl does not proceed via a simple displacive orthorhombic–tetragonal mechanism, but instead displays an order–disorder nature, via an intermediate paraelectric orthorhombic phase. This transition shows both similarities to and differences from that displayed by the Aurivillius phase $Sr_{0.85}Bi_{2.1}Ta_2O_9$.

It is hoped that further detailed studies of both dielectric properties and crystal structure in the Aurivillius and Aurivillius–Sillén intergrowth series will lead to a fuller understanding of their structure–property relationships and, perhaps, a simple parametrization of T_C and P_s vs structural features.

ACKNOWLEDGMENTS

We thank INTAS (Young Scientist Fellowship) and The Royal Society/NATO for awards to AMK, and the EPSRC for provision of neutron diffraction facilities at ISIS. We thank Mr. Charles Hervoches, Dr. K. S. Knight, and Dr. R. I. Smith for their help in the neutron data collection.

REFERENCES

1. C. A. P. de Araujo, J. D. Cuchiaro, L. D. McMillan, M. Scott, and J. F. Scott, *Nature* (*London*) **374,** 627 (1995).
2. F. Abraham, M. F. Debruille-Gresse, G. Mairesse, and G. Nowogrocki, *Solid State Ionics* **28-30,** 529 (1988).
3. B. Aurivillius, *Ark. Kemi.* **1,** 499 (1949).
4. B. Frit and J. P. Mercurio, *J. Alloys Compd* **188,** 27 (1992).
5. V. A. Dolgikh and L. N. Kholodkovskaya, *Russ. J. Inorg. Chem.* **37,** 488 (1992).
6. S. M. Fray, C. J. Milne, and P. Lightfoot, *J. Solid State Chem.* **128,** 115 (1997).
7. B. Aurivillius, *Chem. Scr.* **23,** 143 (1984).
8. J. F. Ackerman, *J. Solid State Chem.* **62,** 92 (1986).
9. A. M. Kusainova, P. Lightfoot, W. Zhou, S. Yu. Stefanovich, A. V. Mosunov, and V. A. Dolgikh, *Chem. Mater.* **13,** 4731 (2001).
10. A. M. Kusainova, S. Yu. Stefanovich, V. A. Dolgikh, A. V. Mosunov, C. H. Hervoches, and P. Lightfoot, *J. Mater. Chem.* **11,** 1141 (2001).
11. A. C. Larson and R. B. von Dreele, Los Alamos National Laboratory Report No. La-UR-86-748, 1987.
12. C. H. Hervoches, J. T. S. Irvine, and P. Lightfoot, *Phys. Rev. B* **64,** 100102(R) (2001).
13. C. H. Hervoches and P. Lightfoot, *Chem. Mater.* **11,** 3359 (1999).
14. C. H. Hervoches and P. Lightfoot, "Proceedings of CIMTEC 2002, 10th International Ceramics Congress," Florence, Italy, July 2002, to appear.
15. A. M. Kusainova, P. S. Berdonosov, L. G. Akselrud, L. N. Kholodkovskaya, V. A. Dolgikh, and B. A. Popovkin, *J. Solid State Chem.* **112,** 189 (1994).
16. B. Aurivillius, *Ark. Kemi.* **4,** 39 (1952).
17. K. G. Keramidas, G. P. Voutsas, and P. I. Rentzeperis, *Z. Kristallogr.* **205,** 35 (1993).
18. J. Ketterer and V. Kraemer, *Acta Crstallogr. C* **42,** 1098 (1986).
19. Y. Shimakawa, Y. Kubo, Y. Nakagawa, T. Kamiyama, H. Asano, and F. Izumi, *Appl. Phys. Lett.* **74,** 1904 (1999).
20. S. C. Abrahams, S. K. Kurtz, and P. B. Jamieson, *Phys. Rev.* **172,** 551 (1968).
21. K. Singh, D. K. Bopardikar, and D. V. Atkare, *Ferroelectrics* **82,** 55 (1988).